Isoscalar $E0$, $E1$, $E2$, and $E3$ strength in ^{92,96,98,100}Mo

D. H. Youngblood,[1] Y.-W. Lui,[1] Krishichayan,[2,3] J. Button,[1] G. Bonasera,[1] and S. Shlomo[1]
[1]*Cyclotron Institute, Texas A&M University, College Station, Texas 77843, USA*
[2]*Department of Physics, Duke University, Durham, North Carolina 27708, USA*
[3]*Triangle Universities Nuclear Laboratory, Durham, North Carolina 27708, USA*
(Received 15 May 2015; published 23 July 2015)

Isoscalar giant resonances in ^{92,96,98,100}Mo have been studied with inelastic scattering of 240-MeV α particles at small angles including 0°. A significant fraction of the energy-weighted sum rule was found for isoscalar $E0$ (107%, 105%, 103%, and 110%), $E1$ (71%, 71%, 70%, and 55%), $E2$ (73%, 69%, 85%, and 79%), and high-energy octupole $E3$ (52%, 65%, 61%, and 53%) resonances in ^{92,96,98,100}Mo, respectively. Spherical Hartree-Fock-based random-phase approximation calculations were performed for each multipole using the KDE0v1 Skyrme-type effective interaction, and the results are compared to the experimental distributions.

DOI: 10.1103/PhysRevC.92.014318 PACS number(s): 25.55.Ci, 24.30.Cz, 27.60.+j

I. INTRODUCTION

The isoscalar giant resonances in the Mo isotopes have received limited study. Moalem *et al.* [1] studied the isoscalar giant quadrupole resonance (GQR) with inelastic scattering of 110-MeV ^{3}He in all of the stable Mo isotopes whereas Duhamel *et al.* [2] reported results for the GQR and the isoscalar giant monopole resonance (GMR) in ^{92}Mo obtained by inelastic scattering of 152-MeV α particles. These analyses assumed Gaussian shapes for both the GQR and the GMR distributions. Recently, we reported a study using inelastic scattering of 240-MeV α particles at small angles including 0° of the GMR in the Zr and Mo isotopes [3] where the $E0$ strength has two components. Because of the excellent peak-to-continuum ratio [4] with the 240-MeV α data, the actual distribution of strength between $E_x = 9$ and 36 MeV can be obtained not only for the GMR, but also for the isoscalar giant dipole resonance (ISGDR), the GQR, and the high-energy octupole resonance (HEOR) as well. In this paper we report $E1$, $E2$, and $E3$ multipole strength distributions obtained for ^{92,96,98,100}Mo and compare the results of spherical Hartree-Fock- (HF-) based random-phase-approximation (RPA) calculations [5] with the KDE0v1 Skyrme-type effective interaction [6].

II. EXPERIMENTAL TECHNIQUE AND DATA ANALYSIS

The experimental technique and detailed method of the analysis have been discussed thoroughly in Ref. [4] and are summarized only briefly below. A beam of 240-MeV α particles from the Texas A&M K500 superconducting cyclotron, after passing through a beam analysis system, bombarded self-supporting target foils 5–8-mg/cm^2 thick enriched to more than 96% in the desired isotope located in the scattering chamber of the multipole-dipole-multipole (MDM) spectrometer. The horizontal and vertical acceptances of the spectrometer were set at 4°. Scattered particles entering the MDM spectrometer were momentum analyzed and measured by a 60-cm-long focal plane detector, which consisted of four resistive wire proportional counters to measure position as well as an ionization chamber to provide ΔE and a plastic scintillator behind the ionization chamber to measure the energy deposited and provide a fast timing signal for the event trigger.

The data for each run were binned into ten angle bins by horizontal angle. The differential cross section was extracted from the number of beam particles collected, the target thickness, the solid angle, the yields measured, and the dead time. The number of beam particles was monitored with a detector at a fixed scattering angle in the scattering chamber. Dead time of the data acquisition system was measured by comparing the number of pulses sent to the system to those accepted. The cumulative uncertainties in the above parameters result in an approximately ±10% uncertainty in absolute cross sections. ^{24}Mg spectra were taken before and after each run, and the (13.85 ± 0.02)-MeV $L = 0$ state [7] was used as a check on the energy calibration in the giant resonance region.

Giant resonance data were taken with the spectrometer at 0.0° (0.0° $< \theta <$ 2.0°) and at 4.0° (2.0° $< \theta <$ 6.0°). Sample spectra obtained for ^{92,96,98,100}Mo are shown in Fig. 1. The giant resonance peaks can be seen extending up past $E_x =$ 30 MeV in all nuclei. The spectra were divided into a peak and a continuum where the continuum was assumed to have the shape of a straight line at high excitation joining onto a Fermi shape at low excitation to model particle threshold effects [4]. Samples of the continua used in the analysis are also shown in Fig. 1.

III. MULTIPOLE ANALYSIS

The multipole components of the giant resonance peak were obtained [4] by dividing the peak into multiple regions (bins) by excitation energy and then comparing the angular distributions obtained for each of these bins to the sum of those calculated for isoscalar 0^+, 1^-, 2^+, 3^-, and 4^+ transitions and the isovector 1^- excitation with distorted-wave Born approximation (DWBA) calculations. Fits to the angular distributions were carried out with a sum of isoscalar 0^+, 1^-, 2^+, 3^-, and 4^+ strengths. The isovector giant dipole resonance contributions were calculated from the known distribution [8] and were held fixed in the fits. The uncertainty from the multipole fits was determined for each multipole by incrementing (or

 ©2015 American Physical Society

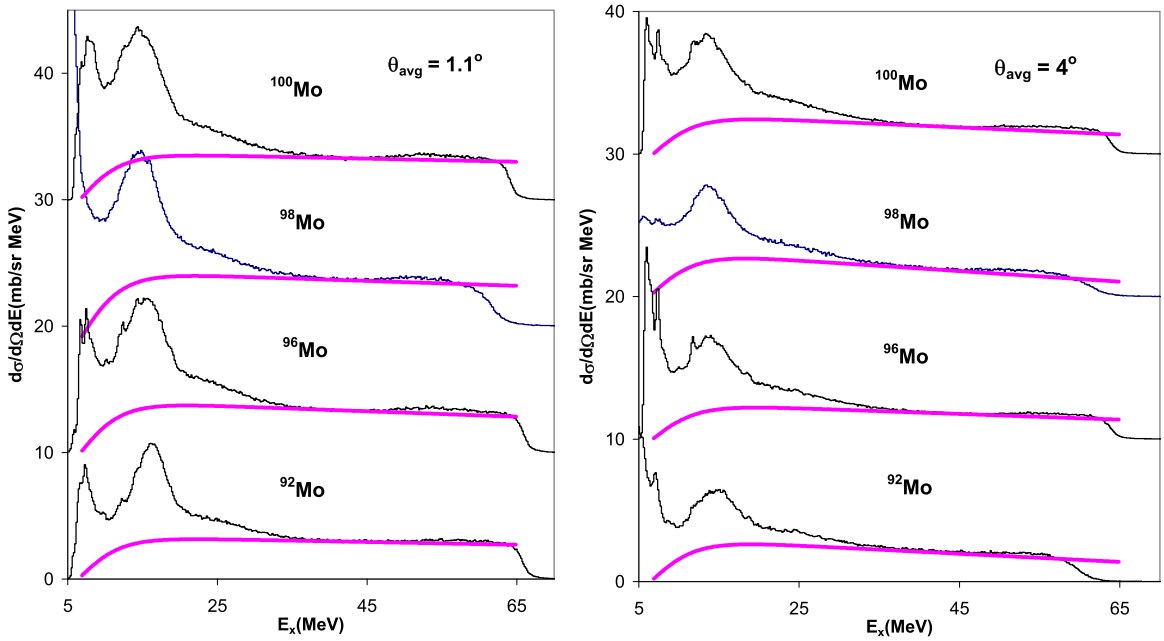

FIG. 1. (Color online) Inelastic α spectra obtained at two angles for ^{92,96,98,100}Mo. The thick pink lines show a continuum chosen for the analysis.

decrementing) that strength, then adjusting the strengths of the multipoles to minimize total χ^2. This continued until the new χ^2 was one unit larger than the total χ^2 obtained for the best fit.

The DWBA calculations were performed [9,10] using the density-dependent single-folding model for the real part, obtained with a Gaussian α-nucleon potential, and a phenomenological Woods-Saxon potential for the imaginary term. These calculations were carried out with the code PTOLEMY [11]. Optical parameters used for the calculations were those determined for elastic scattering of 240-MeV α particles from ^{90}Zr [12] and are given in Table I. The Fermi parameters used for the density distribution of the nuclear ground state were obtained from Ref. [13].

The shape of the real part of the potential and the form factors for PTOLEMY were obtained using the codes SDOLFIN and DOLFIN [14]. The transition densities and sum rules for various multipolarities are discussed thoroughly in Ref. [15] and, except for the ISGDR, the same expressions and techniques were used in this paper. The transition density for inelastic α-particle excitation of the ISGDR given by Harakeh and Dieperink [16] (and described in Ref. [15]) is for only one magnetic substate so that the transition density given in Ref. [15] must be multiplied by $\sqrt{3}$ in the DWBA calculations.

Samples of the angular distributions obtained for the giant resonance peak and the continuum are shown for ^{92}Mo in Fig. 2 and for ^{98}Mo in Fig. 3. Distributions for ^{96}Mo and ^{100}Mo are similar. Sample fits obtained, along with the individual components of the fits, are shown superimposed on the data in Figs. 2 and 3. The continuum distributions are similar over the entire energy range, whereas the angular distributions of the cross sections for the peak change as the contributions of different multipoles dominate in different energy regions.

Several analyses were carried out to assess the effects of different choices of the continuum on the resulting multipole distribution as described in Ref. [17] where the continuum was systematically varied and the data were reanalyzed. The strength distributions obtained from these analyses using different choices of continuum were then averaged, and errors were calculated by adding the errors obtained from the multipole fits in quadrature to the standard deviations between the analyses with different continua. The resulting $E0 - E3$ multipole distributions obtained for ^{92}Mo, ^{96}Mo, ^{98}Mo, and ^{100}Mo are shown in Figs. 4 and 5.

TABLE I. Optical parameters used in DWBA calculations.

V (MeV)	W_i(MeV)	r_i(fm)	a_i(fm)
40.2	40.9	0.786	1.242

IV. DESCRIPTION OF MICROSCOPIC CALCULATIONS

The microscopic mean-field-based RPA theory provides a good description of collective states in nuclei [18,19]. It is common to calculate the RPA states $|n\rangle$ with the corresponding energies E_n and obtain the strength (response) function,

$$S(E) = \Sigma_n |\langle 0|F|n\rangle|^2 \delta(E - E_n),$$

for a certain single-particle scattering operator $F = \Sigma f(i)$ and then determine the energy moments,

$$m_k = \int n E^k S(E) dE.$$

The constrained energy E_{con}, centroid energy E_{cen}, and the scaling energy E_{scal} of the resonance are then obtained from

$$E_{con} = (m_1/m_{-1})^{1/2}, \quad E_{cen} = m_1/m_0, \quad E_{scal} = (m_3/m_1)^{1/2}.$$

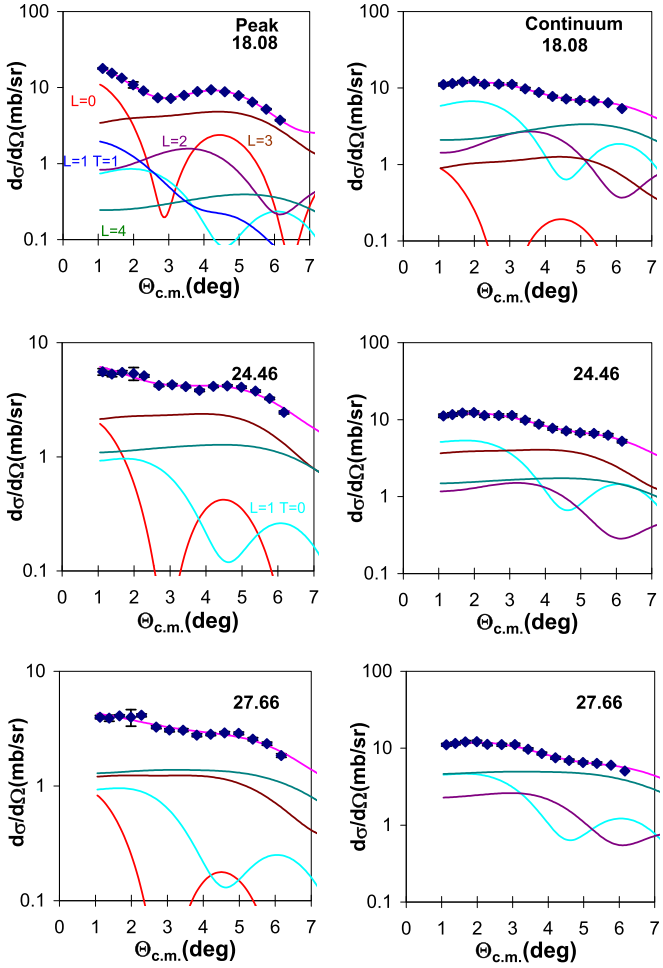

FIG. 2. (Color online) The angular distributions of the ^{92}Mo cross sections for a 500-keV wide bin centered at the excitation energy (in MeV) indicated in each panel for inelastic α scattering for three excitation ranges of the GR peak and the continuum. The lines through the data points indicate the multipole fits. Contributions of each multipole are shown ($L = 0$ red; $L = 1$, $T = 0$ blue-green; $L = 1$, $T = 1$ blue; $L = 2$ maroon; $L = 3$ brown; $L = 4$ green). The statistical errors are shown but in many cases are smaller than the data points.

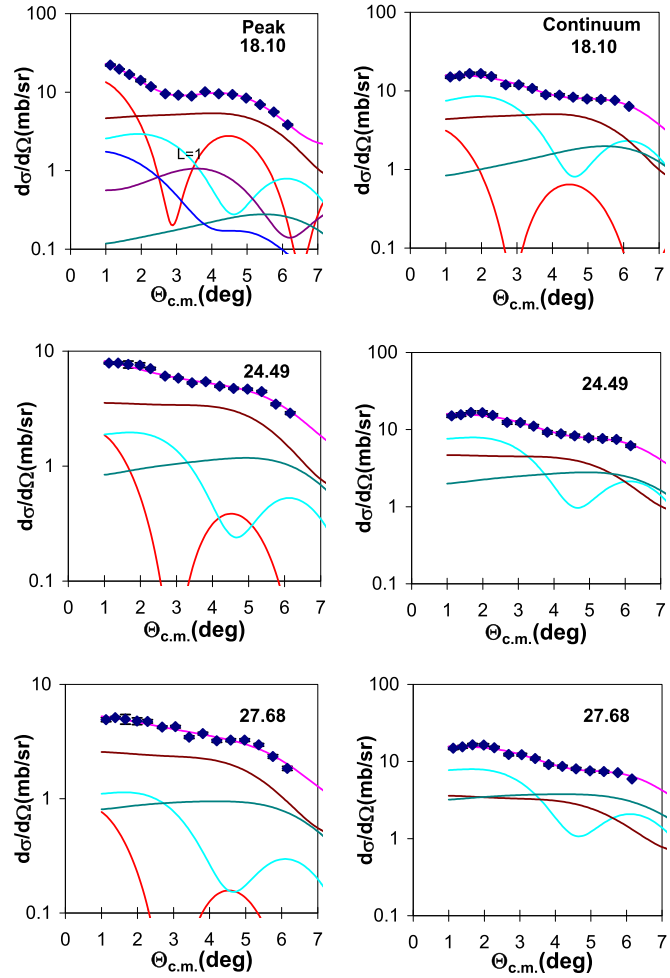

FIG. 3. (Color online) The angular distributions of the ^{98}Mo cross sections. See Fig. 2 caption.

The energy moment m_1 can also be calculated using the HF ground-state wave function, leading to an energy-weighted sum rule (EWSR).

In a fully self-consistent mean-field calculation of the response function, one adopts an effective two-nucleon interaction V, usually fitted to ground-state properties of nuclei and determines the HF mean field. Then, the RPA calculation is carried out with all the components of the two-body interaction using a large configuration space. Employing the numerical approach of Refs. [5,20], we have carried out spherical HF-based RPA calculations of the strength functions and centroid energies of the isoscalar ($T = 0$) giant resonances in ^{92,96,98,100}Mo by employing an occupation number approximation for the single-particle orbits of the open shell nuclei. For the single-particle scattering operator $F = \Sigma_i f(r_i)Y_{LO}$, we used $f(r) = r^2$ for the monopole ($L = 0$) and quadrupole ($L = 2$), $f(r) = r^3$ for the octupole ($L = 3$), and $f(r) = r^3 - \frac{5}{3}\langle r^2\rangle r$ for the dipole ($L = 1$) in order to account for contribution from the spurious state [21,22]. Here we present results obtained using the KDE0v1 Skyrme-type effective interaction, which was fitted to ground-state properties of nuclei, such as binding energy and radii as well as the breathing mode energies of several nuclei [6]. The energy moments of the calculated strength functions were obtained using small smearing widths (0.1 MeV) to ensure accuracy, and they are given in Tables II–V. We used the appropriate experimental excitation energy ranges: ISGMR 9–36 MeV, low component of the ISGDR 9–20 MeV, high component of the ISGDR 20–36 MeV, ISGQR 9–36 MeV, and ISGOR 15–36 MeV when calculating these moments. The calculated distributions using smearing widths of $\Gamma = 10$ MeV for the ISGDR and $\Gamma = 5$ MeV for the other multipoles are shown superimposed on the experimental results in Figs. 4 and 5.

V. DISCUSSION

The $E0-E3$ multipole distributions obtained for ^{92}Mo, ^{96}Mo, ^{98}Mo, and ^{100}Mo are shown in Figs. 4 and 5 along with two (Gaussian) peak fits for the $E0$ and $E1$ distributions,

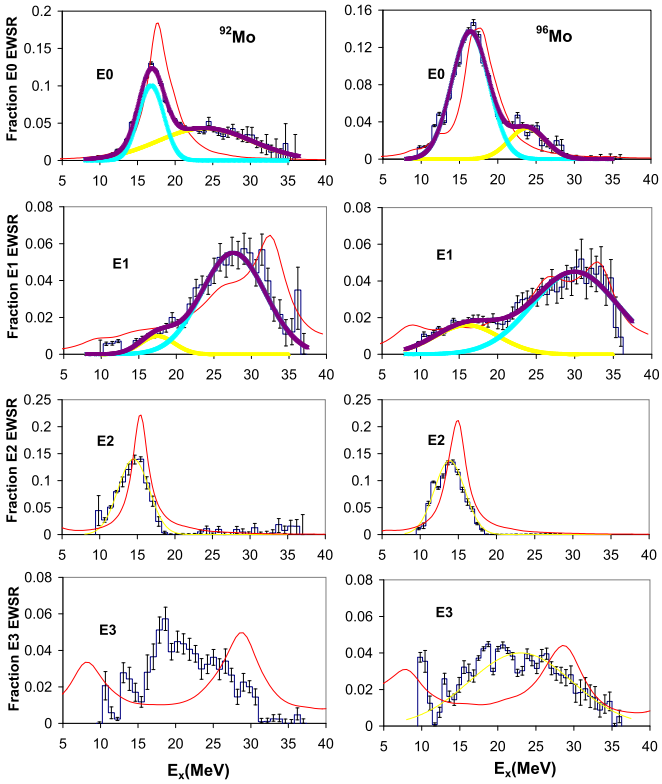

FIG. 4. (Color online) Strength distributions obtained for ^{92}Mo and ^{96}Mo are shown by the histograms. Error bars represent the uncertainty due to the fitting of the angular distributions and different choices of the continuum as described in the text. The thick lines in the $E0$ and $E1$ distributions represent the individual peaks and their sum obtained from the Gaussian fits (the blue and yellow lines are the individual peaks, whereas the brown line indicates the sum). The thin (red) lines are the strength distributions obtained with the HF-RPA calculations using the KDE0v1 interaction, smeared to more closely represent the data as discussed in the text.

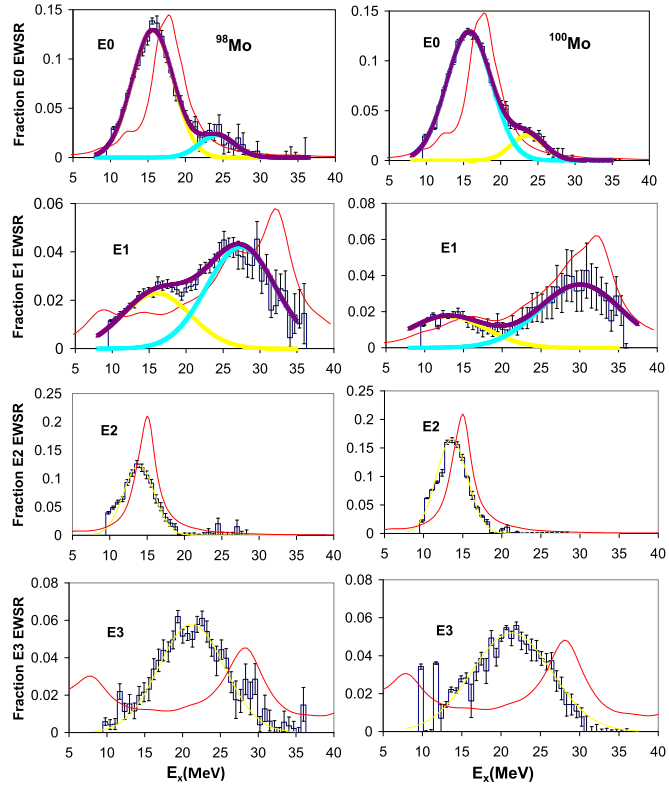

FIG. 5. (Color online) Strength distributions obtained for ^{98,100}Mo are shown by the histograms. See Fig. 4 caption.

whereas single Gaussian fits are shown for each of the $E2$ distributions and the $E3$ distributions for ^{96}Mo, ^{98}Mo, and ^{100}Mo. The $E0$ distributions have been reported previously [3], and the implications of these distributions along with those of the Zr isotopes were explored. Parameters obtained for the moments of the multipole distributions and/or from the Gaussian fits are given in Tables II–V along with those obtained from the KDE0v1 calculations. Each multipole is discussed separately below.

A. $E0$ strength

The $E0$ distributions obtained for the four Mo isotopes have been previously reported [3] and are shown in Figs. 4 and 5. The parameters obtained are summarized in Table II. Each consists of an approximately symmetrical peak between 15.7 and 16.8 MeV with a tail extending up to 30–35 MeV. Also shown in the figures are two-peak fits to the distributions. The $E0$ EWSR strengths obtained are $107 \pm 13\%$, $105 \pm 12\%$, $103 \pm 12\%$, and $110 \pm 12\%$, respectively, for ^{92,96,98,100}Mo. The existence of this high-energy tail (or second peak) was the focus of Ref. [3], but its origin is not understood. The substantial enhancement of the strength in the tail to that in the lower symmetrical peak in both ^{92}Mo and ^{92}Zr results in K_A values for these two nuclei 8σ and 4σ above those obtained with interactions that predict K_A values in agreement with those for the other Zr and Mo isotopes [3]. The results of HF-RPA calculations for the $E0$ strength (broadened with a Lorentzian shape with ∼5-MeV width) are shown superimposed on the data in Figs. 4 and 5. The calculations for each isotope result in a single slightly asymmetrical peak concentrated in a narrow band just above the narrow peak in the data. The energies obtained for the four Mo isotopes from the two peak fits for the low and high components of the $E0$ distributions are plotted versus A in Fig. 6. Also shown are lines representing $74/A^{1/3}$ and $109/A^{1/3}$ on the low and high plots indicating a possible $A^{-1/3}$ dependence of the energies. The energy of the higher peak is essentially constant (within errors) over the mass range of 92–100, however the errors are large enough to possibly mask an $A^{-1/3}$ dependence. The energy of the lower peak clearly decreases somewhat faster than $A^{-1/3}$.

B. Isoscalar $E1$ strength

Much of the expected isoscalar $E1$ strength was identified in the Mo isotopes with strength corresponding to $71 \pm 8\%$, $71 \pm 8\%$, $70 \pm 8\%$, and $55 \pm 7\%$ of the isoscalar $E1$ EWSR located in ^{92}Mo, ^{96}Mo, ^{98}Mo, and ^{100}Mo, respectively, between $E_x =$ 9–36 MeV.

TABLE II. Parameters obtained for the $E0$ distributions shown in Figs. 4 and 5. Uncertainties include systematic errors.

				Gaussian fit						KDE0v1	
				Low peak			High peak				
Nucleus	$\%E0$ EWSR	$(m_3/m_1)^{1/2}$ (MeV)	m_1/m_0 (MeV)	E_x (MeV)	Γ (MeV)	$\%E0$ EWSR	E_x (MeV)	Γ (MeV)	$\%E0$ EWSR	$(m_3/m_1)^{1/2}$ (MeV)	$\%E0$ EWSR
^{92}Mo	107 ± 13	$21.68^{+0.53}_{-0.33}$	$19.62^{+0.28}_{-0.19}$	16.8	4.0	42	23.9	14.7	65	18.51	99.43
^{96}Mo	105 ± 12	$18.18^{+0.20}_{-0.13}$	$16.95^{+0.12}_{-0.10}$	16.4	5.7	83	23.8	5.7	20	18.04	98.36
^{98}Mo	103 ± 12	$17.29^{+0.46}_{-0.21}$	$16.01^{+0.19}_{-0.13}$	15.7	6.5	89	24.2	5.6	14	18.07	98.10
^{100}Mo	110 ± 12	$17.35^{+0.16}_{-0.12}$	$16.13^{+0.11}_{-0.10}$	15.8	7.1	97	23.6	5.5	14	17.89	99.28

TABLE III. Parameters obtained for the isoscalar $E1$ distributions shown in Figs. 4 and 5. Uncertainties include systematic errors.

		Gaussian fit						KDE0v1			
	Total	Low peak			High peak			Low peak		High peak	
Nucleus	$\%E1$ EWSR	E_x (MeV)	Γ (MeV)	$\%E1$ EWSR	E_x (MeV)	Γ (MeV)	$\%E1$ EWSR	m_1/m_0 (MeV)	$\%E1$ EWSR	m_1/m_0 (MeV)	$\%E1$ EWSR
^{92}Mo	71 ± 8	17.5 ± 0.4	5.4 ± 0.7	5.8 ± 1.1	27.6 ± 0.5	10.2 ± 2.0	59 ± 7	13.46	13.95	28.81	75.58
^{96}Mo	71 ± 8	15.9 ± 0.3	10.1 ± 1.1	17 ± 2	30.0 ± 0.7	13.1 ± 2.9	62 ± 8	14.30	15.05	28.37	69.22
^{98}Mo	70 ± 8	16.0 ± 0.3	10.9 ± 1.1	26 ± 3	27.4 ± 0.7	10.8 ± 3.0	49 ± 8	14.02	15.06	28.36	70.01
^{100}Mo	55 ± 7	13.0 ± 0.3	11.6 ± 1.2	18 ± 3	30.1 ± 0.7	12.5 ± 3.8	47 ± 10	14.50	13.99	28.37	71.10

TABLE IV. Parameters obtained for the isoscalar $E2$ distributions shown in Figs. 4 and 5. Uncertainties include systematic errors.

				Gaussian fit		KDE0v1	
Nucleus	$\%E2$ EWSR	m_1/m_0 (MeV)	RMS width (MeV)	E_x (MeV)	Γ (MeV)	m_1/m_0 (MeV)	$\%E2$ EWSR
^{92}Mo	73 ± 13	14.16 ± 0.25	2.03 ± 0.30	14.51 ± 0.23	4.84 ± 0.35	15.44	93.48
^{96}Mo	69 ± 13	13.61 ± 0.24	1.80 ± 0.25	13.85 ± 0.25	4.70 ± 0.37	14.78	97.18
^{98}Mo	85 ± 14	13.53 ± 0.23	2.80 ± 0.26	13.85 ± 0.24	4.68 ± 0.34	14.77	97.45
^{100}Mo	79 ± 14	13.46 ± 0.26	1.91 ± 0.26	13.60 ± 0.26	4.75 ± 0.38	14.76	97.18
		Ref. [1]				Ref. [2]	
	$\%E2$	E_x	Γ		$\%E2$	E_x	Γ
Nucleus	EWSR	(MeV)	(MeV)		EWSR	(MeV)	(MeV)
^{92}Mo	84 ± 17	15.1 ± 0.4	5.0 ± 0.4		23 ± 5	14.1 ± 0.2	4.55 ± 0.34
^{96}Mo	72 ± 14	14.2 ± 0.2	5.0 ± 0.3				
^{98}Mo	87 ± 17	14.2 ± 0.4	4.7 ± 0.4				
^{100}Mo	88 ± 18	13.7 ± 0.2	5.2 ± 0.3				

TABLE V. Parameters obtained for the isoscalar $E3$ strength above $E_x = 15$ MeV shown in Figs. 4 and 5. Uncertainties include systematic errors.

				KDE0v1	
Nucleus	$\%E3$ EWSR	m_1/m_0 (MeV)	RMS width (MeV)	m_1/m_0 (MeV)	$\%E3$ EWSR
^{92}Mo	52 ± 7	21.8 ± 0.4	4.3 ± 0.3	26.99	63.85
^{96}Mo	65 ± 9	21.4 ± 0.4	5.8 ± 0.4	26.35	60.66
^{98}Mo	61 ± 8	21.5 ± 0.4	4.2 ± 0.3	26.27	61.01
^{100}Mo	53 ± 7	21.5 ± 0.4	3.7 ± 0.3	26.11	61.80

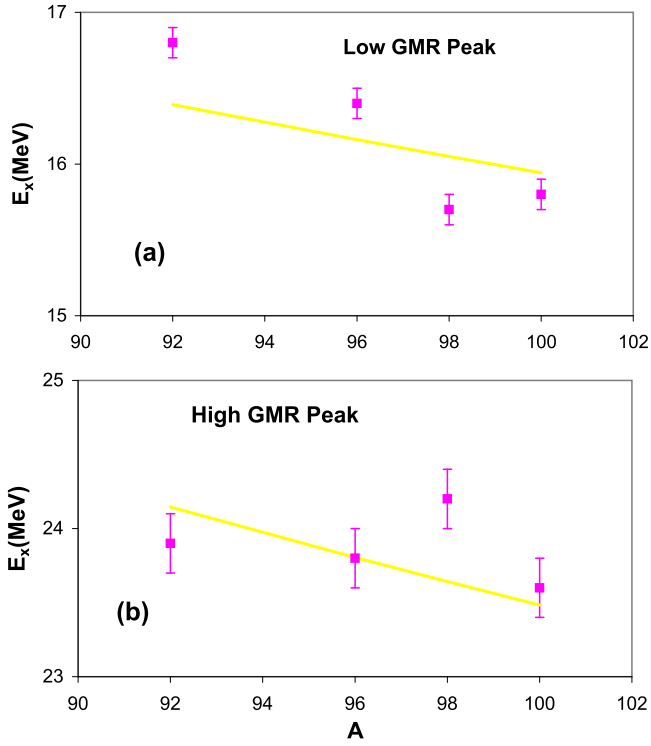

FIG. 6. (Color online) The centroids of the Gaussians obtained from the fits to the $E0$ distributions for the Mo isotopes are plotted versus A. The error bars indicate the uncertainty obtained using the errors shown in Figs. 4 and 5. The (yellow) lines show (a) $74/A^{-1/3}$ and (b) $109/A^{-1/3}$ in two plots.

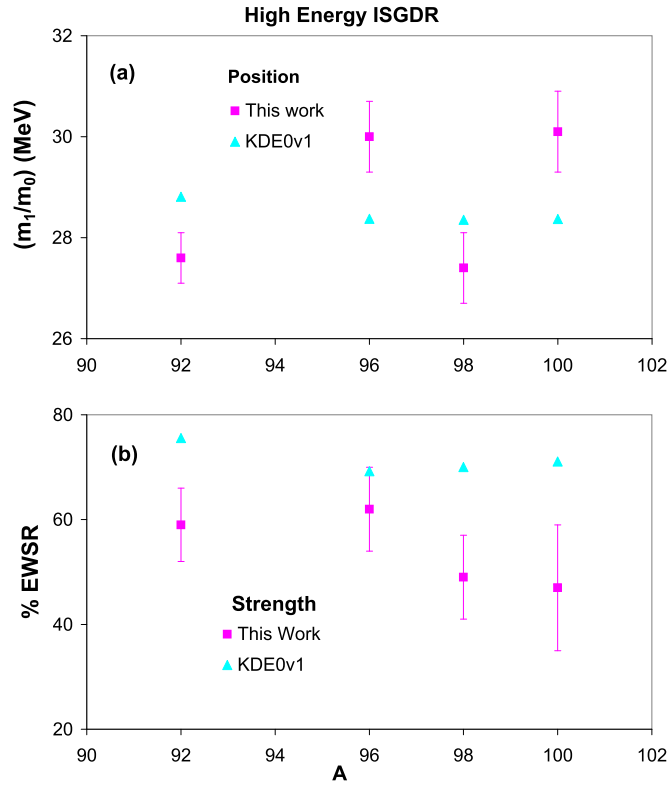

FIG. 7. (Color online) The centroid of the Gaussian fit to the high-energy peak in the ISGDR distributions for each of the Mo isotopes is plotted versus A in (a) whereas the strength of the upper peak is plotted in (b). The error bars indicate the uncertainty obtained using the errors shown in Figs. 4 and 5. The triangles (blue) show m_1/m_0 for the strength between $E_x = 20$ MeV and $E_x = 36$ MeV calculated with HF-RPA using the KDE0v1 interaction.

The isoscalar dipole is split into $1\hbar\omega$ and $3\hbar\omega$ components [23–25], and the upper component is expected to be a compression mode whose energy is related to the compression modulus K_A of the nucleus. Two-peak Gaussian fits were made to the distributions shown in Figs. 4 and 5. The fits are shown in the figures, and the parameters obtained are listed in Table III. There are no previous reports of the ISGDR in the Mo isotopes. HF-RPA calculations with the KDE0v1 interaction are shown superimposed on the multipole distributions in Figs. 4 and 5. The HF-RPA calculations show 14% to 15% of the ISGDR EWSR in the range of $E_x = 9$–20 MeV (mostly the $1\hbar\omega$ component) with $m_1/m_0 \sim 14$MeV and 69%–76% of the ISGDR EWSR in the range of $E_x = 20$–36 MeV (the $3\hbar\omega$ component) with $m_1/m_0 \sim 28.5$ MeV. For ^{92}Mo and ^{98}Mo, the strongest peak in the calculation is at approximately $E_x = 32.5$–33 MeV whereas the data peak around 26–28 MeV and are substantially lower than the calculation in the 34–36-MeV region. For ^{96}Mo and ^{100}Mo the experimental and calculated distributions are in fairly good agreement (within the errors), although the strength seen in ^{100}Mo is a little low. The strengths and Gaussian centroids of the high-energy peaks are compared to those obtained from the HF-RPA calculations in Table III and Fig. 7. Except for ^{96}Mo, the strength seen experimentally is somewhat less than predicted to lie in this energy range.

C. $E2$ strength

The $E2$ strengths in ^{92}Mo, ^{96}Mo, ^{98}Mo, and ^{100}Mo, summarized in Table IV, are concentrated in (almost) Gaussian peaks centered between 13.5 and 14.2 MeV containing $73 \pm 13\%$, $69 \pm 13\%$, $85 \pm 14\%$, and $79 \pm 14\%$ of the $E2$ EWSR, respectively. The peaks were fitted with Gaussians and m_1/m_0, the rms width, and the Gaussian parameters are given. The peaks are a little asymmetric with extra yield on the low-energy side, so the Gaussian energies are a few hundred keV higher than m_1/m_0. Moalem *et al.* [1] measured the GQR in ^{92,94,96,98,100}Mo with inelastic scattering of 110-MeV ^{3}He, and our results for % EWSR, energy, and width agree within the errors with their work. Duhamel *et al.* [2] measured the GQR in ^{92}Mo with inelastic scattering of 120-MeV α particles and obtained an energy and width in agreement with our result but only identified $23 \pm 5\%$ of the $E2$ EWSR strength. Figure 8 compares the (Gaussian) energy of the GQR in the Mo isotopes obtained from the three experiments and m_1/m_0 obtained from the calculation with the KDE0v1 interaction. The calculated energies are ~1 MeV higher than our experimental energies. The position of the GQR is sensitive [26] to the effective mass (0.74 in KDE0v1), and a higher effective mass would lower the predicted GQR energy, obtaining agreement with

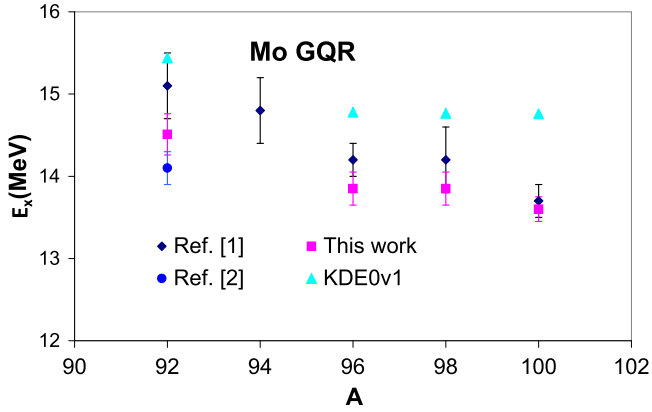

FIG. 8. (Color online) The centroid of the $E2$ strength in each of the Mo isotopes obtained in this work (red squares) is plotted versus A. The error bars indicate the uncertainty obtained using the errors shown in Figs. 4 and 5. Also shown with error bars are centroids reported in Ref. [1] (black diamonds) and a measurement for ^{92}Mo [2] (blue circle). The light blue triangles show the centroid of the $E2$ strength obtained from HF-RPA calculations with the KDE0v1 interaction.

data with effective masses of ∼0.8, see Ref. [27] for a more detailed investigation.

D. $E3$ strength

In the harmonic-oscillator shell model, $E3$ strength in a nucleus is split into a $1\hbar\omega$ low-energy-octupole resonance (LEOR) containing 25% of the isoscalar $E3$ EWSR and a $3\hbar\omega$ high-energy-octupole resonance (HEOR) containing 75% of the EWSR [28], however coupling these modes with an octupole-octupole residual interaction results in the LEOR having ∼35% of the $E3$ EWSR and the HEOR having ∼65%. Our low-energy cutoff in this experiment lies in the middle to higher region of the LEOR so that we are unable to extract useful parameters for the LEOR. The observed $E3$ strength distributions (Figs. 4 and 5) are broadly spread from $E_x \sim 9$ MeV (the lower threshold of our detector) and taper off between $E_x = 30$–35 MeV before reaching the upper limit of the region we observe ($E_x \sim 36$ MeV). We arbitrarily assign to the HEOR that strength lying above $E_x = 12$–15 MeV depending on the apparent gap in the strength distributions, and the strengths, m_1/m_0, and rms widths for the data above this division are listed in Table V along with m_1/m_0 and the strengths calculated with KDE0v1 over the range of 15–36 MeV. There are no previous reports of the HEOR in the Mo isotopes. The isoscalar $E3$ strength calculated with the KDE0v1 interaction is also shown in Figs. 4 and 5 and has peaks at ∼8 MeV (the LEOR) and at ∼29 MeV (the HEOR) whereas the experimental strength lies in a broad peak centered at ∼21.5 MeV. The experimental and calculated energies and strengths are compared in Fig. 9. The excitation energy (m_1/m_0) we obtain for each of the isotopes is near 21.5 MeV, well below the ∼26.1–27.0 MeV obtained with the HF-RPA calculations. The centroid (m_1/m_0) obtained from the HF-RPA calculations for the strength lying above $E_x = 15$ MeV of the $E3$ is 2 to 3 MeV below the ∼29-MeV peak position because

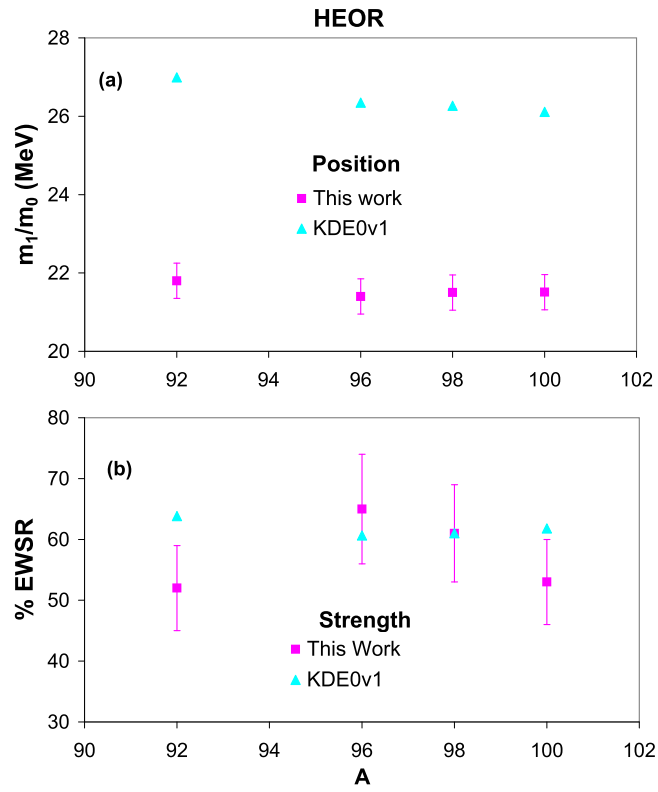

FIG. 9. (Color online) The centroid of the $E3$ strength observed above $E_x = 15$ MeV for each of the Mo isotopes in this work (red squares) is plotted versus A in (a), whereas the strength in this region is plotted in (b). The error bars indicate the uncertainty obtained using the errors shown in Figs. 4 and 5. The large light blue triangles show (a) the centroid and (b) the % EWSR of the $E3$ strength between $E_x = 15$ MeV and $E_x = 36$ MeV obtained from HF-RPA calculations with the KDE0v1 interaction.

there is significant strength in the 15–20-MeV range. The strengths obtained for the HEOR in the HF-RPA calculations range from 60.7% to 63.9% of the $E3$ EWSR, in agreement within the errors with data for ^{96}Mo and ^{98}Mo. The observed $E3$ strengths for ^{92}Mo ($52 \pm 7\%$) and ^{100}Mo ($53 \pm 7\%$) are somewhat lower than the 63.85% and 61.80% obtained with the KDE0v1 interaction. The energies of the HEOR and the GQR are sensitive to the effective mass [26], and a larger effective mass would result in a lower energy for both these excitations.

VI. SUMMARY

We have obtained distributions for isoscalar $E0$, $E1$, $E2$, and $E3$ strength containing 52%–110% of the expected strength in ^{92}Mo, ^{96}Mo, ^{98}Mo, and ^{100}Mo and compared these to spherical Hartree-Fock-RPA calculations using the KDE0v1 Skyrme-type interaction. As discussed in a previous report [3], the $E0$ strength has a high-energy tail which contains a substantially larger fraction of the $E0$ strength in ^{92}Mo than the other isotopes which shifts the GMR energy substantially higher for ^{92}Mo, a shift not seen in the HF-RPA calculation. The source of this tail, not present in heavier nuclei, is not

understood, and the distributions for the other multipoles do not differ substantially between the isotopes. The position of the high-energy part of the isoscalar dipole agrees reasonably well with the HF-RPA calculation. The position, strength, and width of the $E2$ distributions agree within errors with those obtained by Moalem *et al.* [1] but are ∼1 MeV below those obtained with the HF-RPA calculations. The HEOR strength lies in a broad peak centered at ∼21.5 MeV in each isotope, approximately 4 MeV below that obtained with the HF-RPA calculations. We will follow up with a study, similar to an earlier one for ^{40}Ca and ^{48}Ca [26], which found the $E2$ and $E3$ centroids most sensitive to the effective mass m^*/m by carrying out self-consistent HF-RPA calculations using a number of interactions.

ACKNOWLEDGMENTS

This work was supported, in part, by the U.S. Department of Energy under Grant No. DE-FG03-93ER40773.

[1] A. Moalem, Y. Gaillard, A. M. Bemolle, M. Buenerd, J. Chauvin, G. Duhamel, D. Lebrun, P. Martin, G. Perrin, and P. de Saintignon, Phys. Rev. C **20**, 1593(R) (1979).
[2] G. Duhamel, M. Buenerd, P. de Saintignon, J. Chauvin, D. Lebrun, P. Martin, and G. Perrin, Phys. Rev. C **38**, 2509 (1988).
[3] D. H. Youngblood, Y.-W. Lui, Krishichayan, J. Button, M. R. Anders, M. L. Gorelik, M. H. Urin, and S. Shlomo, Phys. Rev. C **88**, 021301(R) (2013).
[4] D. H. Youngblood, Y.-W. Lui, and H. L. Clark, Phys. Rev. C **65**, 034302 (2002); **63**, 067301 (2001); **61**, 067307 (2000); **60**, 014304 (1999).
[5] P.-G. Reinhardt, Ann. Phys. (Leipzig) **504**, 632 (1992).
[6] B. K. Agrawal, S. Shlomo, and V. K. Au, Phys. Rev. C **72**, 014310 (2005).
[7] K. van der Borg, M. N. Harakeh, and A. van der Woude, Nucl. Phys. **A365**, 243 (1981).
[8] S. S. Dietrich and B. L. Berman, At. Data Nucl. Data Tables **38**, 199 (1988).
[9] G. R. Satchler and Dao T. Khoa, Phys. Rev. C **55**, 285 (1997).
[10] H. L. Clark, Y.-W. Lui, and D. H. Youngblood, Phys. Rev. C **57**, 2887 (1998).
[11] M. Rhoades-Brown, M. H. Macfarlane, and S. C. Pieper, Phys. Rev. C **21**, 2417 (1980); M. H. Macfarlane and S. C. Pieper, Argonne National Laboratory Report No. ANL-76-11, 1978 (unpublished).
[12] H. L. Clark, Y.-W. Lui, and D. H. Youngblood, Nucl. Phys. A **687**, 80c (2000).
[13] G. Fricke, C. Bernhardt, K. Heilig, L. A. Schaller, L. Schellenberg, E. B. Shera, and C. W. Dejager, At. Data Nucl. Data Tables **60**, 177 (1995).
[14] L. D. Rickerston, The folding program DOLFIN, 1976 (unpublished).
[15] D. H. Youngblood, Y.-W. Lui, and H. L. Clark, Phys. Rev. C **55**, 2811 (1997).
[16] M. N. Harakeh and A. E. L. Dieperink, Phys. Rev. C **23**, 2329 (1981).
[17] D. H. Youngblood, Y.-W. Lui, H. L. Clark, B. John, Y. Tokimoto, and X. Chen, Phys. Rev. C **69**, 034315 (2004).
[18] A. Bohr and B. M. Mottelson, *Nuclear Structure II* (Benjamin, New York, 1975).
[19] S. Shlomo, V. M. Kolomietz, and G. Colo, Eur. Phys. J. A **30**, 23 (2006), and references therein.
[20] Tapas Sil, S. Shlomo, B. K. Agrawal, and P.-G. Reinhard, Phys. Rev. C **73**, 034316 (2006).
[21] S. Shlomo and A. I. Sanzhur, Phys. Rev. C **65**, 044310 (2002).
[22] B. K. Agrawal, S. Shlomo, and A. I. Sanzhur, Phys. Rev. C **67**, 034314 (2003).
[23] H. L. Clark, Y.-W. Lui, and D. H. Youngblood, Phys. Rev. C **63**, 031301(R) (2001).
[24] G. Colo, N. Van Giai, P. F. Bortignon, and M. R. Quaglia, Phys. Lett. B **485**, 362 (2000).
[25] D. Vretenar, A. Wandelt, and P. Ring, Phys. Lett. B **487**, 334 (2000).
[26] M. R. Anders, S. Shlomo, Tapas Sil, D. H. Youngblood, Y.-W. Lui, and Krishichayan, Phys. Rev. C **87**, 024303 (2013).
[27] G. Bonasera *et al.* (unpublished).
[28] J. M. Moss, D. H. Youngblood, C. M. Rozsa, D. R. Brown, and J. D. Bronson, Phys. Rev. Lett. **37**, 816 (1976).